Advantage of hyperspectral EO-1 Hyperion over multispectral IKONOS, GeoEye-1, WorldView-2, Landsat ETM+, and MODIS vegetation indices in crop biomass estimation

Michael Marshall [a,b,*], Prasad Thenkabail [b]

[a] Climate Research Unit, World Agroforestry Centre, United Nations Ave, Gigiri, P.O. Box 30677-00100, Nairobi, Kenya
[b] Southwestern Geographic Center, Geological Survey, 2255 N. Gemini Dr, Flagstaff, AZ, USA

ABSTRACT

Crop biomass is increasingly being measured with surface reflectance data derived from multispectral broadband (MSBB) and hyperspectral narrowband (HNB) space-borne remotely sensed data to increase the accuracy and efficiency of crop yield models used in a wide array of agricultural applications. However, few studies compare the ability of MSBBs versus HNBs to capture crop biomass variability. Therefore, we used standard data mining techniques to identify a set of MSBB data from the IKONOS, GeoEye-1, Landsat ETM+, MODIS, WorldView-2 sensors and compared their performance with HNB data from the EO-1 Hyperion sensor in explaining crop biomass variability of four important field crops (rice, alfalfa, cotton, maize). The analysis employed two-band (ratio) vegetation indices (TBVIs) and multiband (additive) vegetation indices (MBVIs) derived from Singular Value Decomposition (SVD) and stepwise regression. Results demonstrated that HNB-derived TBVIs and MBVIs performed better than MSBB-derived TBVIs and MBVIs on a per crop basis and for the pooled data: overall, HNB TBVIs explained 5–31% greater variability when compared with various MSBB TBVIs; and HNB MBVIs explained 3–33% greater variability when compared with various MSBB MBVIs. The performance of MSBB MBVIs and TBVIs improved mildly, by combining spectral information across multiple sensors involving IKONOS, GeoEye-1, Landsat ETM+, MODIS, and WorldView-2. A number of HNBs that advance crop biomass modeling were determined. Based on the highest factor loadings on the first component of the SVD, the "red-edge" spectral range (700–740 nm) centered at 722 nm (bandwidth = 10 nm) stood out prominently, while five additional and distinct portions of the recorded spectral range (400–2500 nm) centered at 539 nm, 758 nm, 914 nm, 1130 nm, 1320 nm (bandwidth = 10 nm) were also important. The best HNB vegetation indices for crop biomass estimation involved 549 and 752 nm for rice ($R^2 = 0.91$); 925 and 1104 nm for alfalfa ($R^2 = 0.81$); 722 and 732 nm for cotton ($R^2 = 0.97$); and 529 and 895 nm for maize ($R^2 = 0.94$). The higher spectral resolution of the EO-1 Hyperion hyperspectral sensor and the ability of users to choose distinct HNBs for improved crop biomass estimation outweigh the benefits that come with higher spatial resolution of MSBBs.

1. Introduction

Changes in biomass density vary proportionally to the quantity of carbon that is gained or lost by vegetation via photosynthesis, respiration, growth, and decay, making it an important indicator of natural and anthropogenic greenhouse (GHG) forcing on the atmosphere and climate change (Houghton et al., 2009). Agriculture accounts for approximately 25% of the global GHG budget (Stocker et al., 2013). Carbon emissions from agriculture are second to emissions from fossil fuel consumption and result primarily from the conversion of natural forests and grasslands to croplands and pastures, respectively (Vermeulen et al., 2013). Direct or *in situ* estimates of carbon stocks in these transition zones, though important for estimating the global carbon balance, remain highly uncertain, due to temporal variations (disturbance/recovery) and spatial heterogeneity of the landscape (Houghton,

---

* Corresponding author at: Climate Research Unit, World Agroforestry Centre, United Nations Ave, Gigiri, P.O. Box 30677-00100, Nairobi, Kenya. Tel.: +254207224244 (O).
E-mail addresses: m.marshall@cgiar.org (M. Marshall), pthenkabail@usgs.gov (P. Thenkabail).

2010). Agro-ecosystem models, typically calibrated with *in situ* biophysical and/or biochemical data, are used to model biomass consistently over large areas at various spatio-temporal scales. Many agro-ecosystem models are parameterized with remote sensing spectral information, because it facilitates the frequent and rapid retrieval of biophysical and biochemical properties over multiple spatial scales and often in inaccessible areas (Lu, 2006). Given the large number of remote sensors (each with distinct spectral, spatial, and radiometric properties) studies that compare and contrast their ability to estimate crop biomass can help reduce uncertainties in biomass estimates and ultimately carbon flux estimates.

Dorigo et al. (2007) reviews of methods for estimating biophysical and biochemical properties from remote sensing spectral information in agro-ecosystem modeling, including crop biomass. Plant chlorophyll absorbs strongly in the visible red (620–700 nm) and transitions rapidly in a region known as the "red-edge" (700–740 nm) to reflect/transmit strongly in the near infrared (NIR: 740–1000 nm) due to plant cellular structure. Given this response, early attempts to measure biomass with remote sensing focused on red-NIR vegetation indices. The most commonly used of these is the Normalized Difference Vegetation Index (NDVI) (Tucker, 1979). Red-NIR vegetation indices attempt to enhance the vegetation signal and reduce the effects of soil background and solar irradiance (Elvidge and Chen, 1995), but remain sensitive to soil wetness and other noises, particularly at coarser spatial resolution (Huete et al., 2002). Therefore other methods have been developed that fall into two broad categories: empirical and semi-physical. Empirical methods typically involve relating biomass to transformed spectral information via band ratioing or stepwise linear regression (e.g. Mariotto et al., 2013), partial least squares regression (e.g. Hansen and Schjoerring, 2003), or artificial neural networks (e.g. Serele et al., 2000). Although empirical methods are accurate in the area they are developed, simple, and computationally undemanding, model transferability is often difficult. Semi-physical methods involve the inversion of coupled radiative transfer and biochemical models, such as PROSAIL (Casa and Jones, 2004). These models in the "forward" mode are driven by biophysical and biogeochemical parameters to estimate the spectral properties of a canopy. In the "inverted" mode, spectra can be used to estimate the biophysical and biogeochemical determinants of biomass in a cause-and-effect manner, increasing the likelihood of transferability (Jacquemoud et al., 1995). However, these models require several inputs and are sensitive to canopy architecture (i.e. clumping), and the inversion procedure is not trivial (Jacquemoud et al., 2009).

The spectral data used to estimate crop biomass involves one of two sensor types in the optical range: multispectral broadband (MSBB) and hyperspectral narrowband (HNB). Multispectral broadband data can be further classified into high (e.g. IKONOS), medium (e.g. Landsat), and coarse (e.g. MODIS) spatial resolution. High spatial resolution images are less affected by spatial heterogeneity than medium and coarse resolution images, but they must be purchased on-demand, require greater computational resources, and (with the exception of new deployments; e.g. WorldView-3: http://worldview3.digitalglobe.com/) contain fewer spectral bands (Thenkabail, 2004). Medium to coarse resolution remote sensing images, on the other hand, are freely available, provide global coverage at a frequent (16-day to daily) return interval, require little additional processing, and have a higher spectral resolution. Hyperspectral narrowband data are currently derived from only one active space-borne sensor: Hyperion onboard Earth Observing-1 (EO-1). Unlike MSBBs, it yields spectral information at discrete 10 nm intervals over a wide optical range (350–2500 nm) freely on-demand (Thenkabail et al., 2013). The level of spectral detail afforded by EO-1 enhances vegetation characteristics that are difficult to discriminate with MSBBs. A review of these characteristics can be found in Goetz (2009) and Ustin et al. (2004). They include pigment concentration (chlorophylls, carotenoids, and anthocyanins) detected in the visible range (450–700 nm) (Gitelson et al., 2006); leaf nitrogen content detected in the red-edge (700–740 nm) (Perry and Roberts, 2008), canopy water content detected in the SWIR1 (1000–1700 nm) (Carter, 1991), and canopy dry plant litter or wood (lignose/cellulose) detected in the SWIR2 (1700–2500 nm) (Asner, 1998). The major drawback of HNBs is the large number of bands involved and necessity for data mining techniques to interpret the data. The merging of MSBBs and HNBs could overcome some of the spectral, spatial, and radiometric limitations of methods that use only MSBBs or HNBs, but remains a relatively unexplored topic (Thenkabail et al., 2004).

Given the lack of studies that report the relative ability of HNBs and MSBBs to estimate crop biomass, either individually or in combination, this study uses a suite of Hyperion HNBs; several high, medium, and coarse spatial resolution MSBBs; and field estimates of aboveground wet biomass (**AWB**) retrieved for field crops to identify an optimal set of HNBs and MSBBs that maximize explained biomass variability on a per-crop basis and for the pooled data. We use **AWB**, which only includes the fresh-weight aboveground portion of the crop, because retrieval is less labor intensive and it correlates well with the dry biomass of field crops (Thenkabail et al., 1994).

2. Study area

California is considered the most agriculturally diverse and productive state in the United States (US): it produces more than 350 agricultural commodities and accrued cash receipts from agricultural production amounting to 44.7 billion dollars or 11.3% of total agricultural receipts in the US in 2012 (http://www.nass.usda.gov/). The Central Valley of California (Fig. 1) covers an area of nearly 60,000 km^2 (13.7% of the state's total land area) and includes eight of California's most agriculturally productive counties (in descending order): Fresno, Tulare, Kern, San Joaquin, Merced, Stanislaus, San Joaquin, and Kings (Umbach, 1997). Irrigation water use in agricultural production accounts for approximately 75% of California's annual water budget (Kenny et al., 2009). Climate change (Dettinger et al., 2004), rapid population growth (http://www.census.gov/), and expanding agricultural land use (Soulard and Wilson, 2013) have led to surface and groundwater withdrawals that are projected to reach unstainable levels by mid-21st century (Spencer and Altman, 2010).

In 2012, spectral information was retrieved from several earth observation platforms and co-located with ground-based estimates of **AWB** in the Central Valley. The farms where **AWB** was measured were either privately owned or managed by University of California at Davis Research and Extension Centers or the California Department of Water Resources. The farms were stratified across the Central Valley to account for different climate, soil, and irrigation regimes. The purpose of the field survey was to develop a series of **AWB** transects that accounted for spatial heterogeneity and facilitated the identification of an optimal set of space-borne MSBBs and HNBs that captured the most **AWB** variability. Image-**AWB** pairs included California's four largest crop water consumers (alfalfa, cotton, maize, and rice) (http://www.water.ca.gov/) during the three primary phases of crop development (sprouting, flowering/silking, and boll/grain-filling), yielding nearly 250 samples for the analysis. Preprocessing steps were taken to georectify and normalize the remote sensing data for inter-sensor comparison.
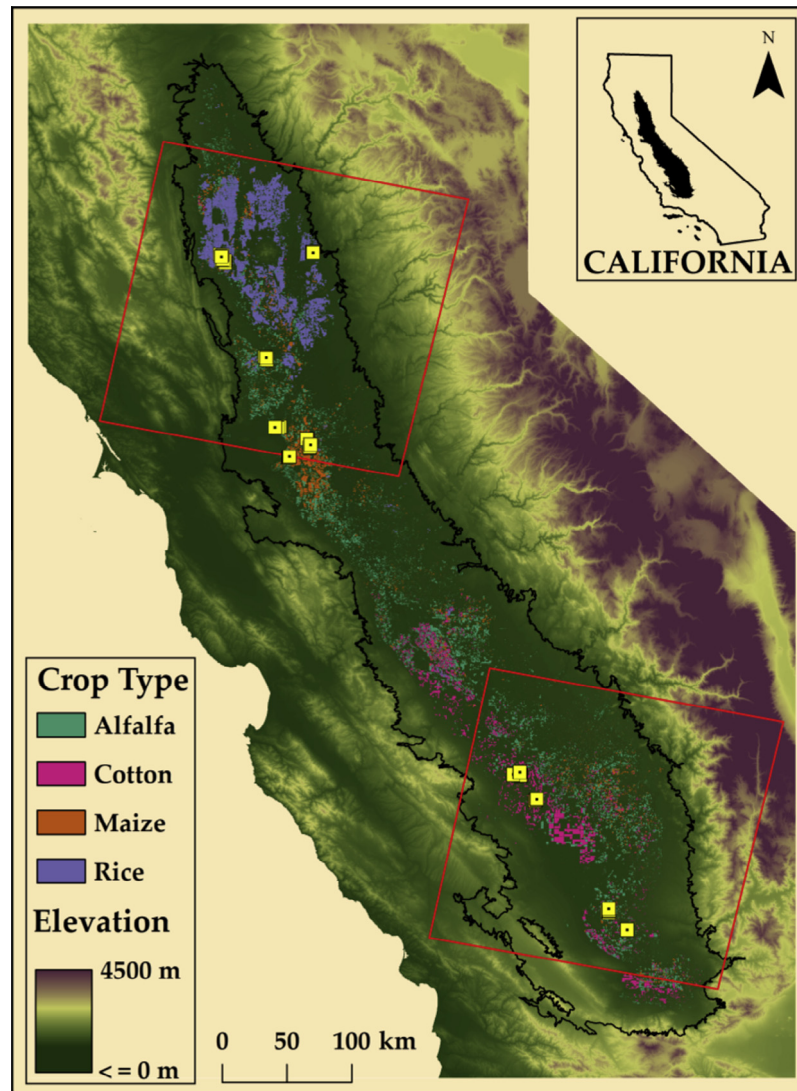
Fig. 1. The central valley of California. One hundred and twenty 60 × 60 m transects (■) were developed to estimate aboveground wet biomass (**AWB**) for California's most water intensive crops (alfalfa, cotton, maize, and rice) in 2012. The transects were visited during the sprouting, flowering/silking, and bud/grain-filling phases of crop development. The upper (path/row = 44, 33) and lower (path/row = 42, 35) extent of Landsat ETM + scenes used to develop predictive models of **AWB** are outlined in red. The extent of crop cover was downloaded from the National Agricultural Statistics Service Cropland Data Layer (http://nassgeodata.gmu.edu/) for 2012, while elevation is a subset of the 30 m resolution National Elevation Dataset (http://nationalmap.gov/). (For interpretation of the references to color in this figure legend, the reader is referred to the web version of this article.)

3. Data and methods

3.1. Ground reference data

Marshall and Thenkabail (2015) details the development of **AWB** (g m^{-2}) transects used to evaluate the MSBB and HNB vegetation indices in this study. Each transect, randomly distributed over 18 farms across the Central Valley during 2011 and 2012, represent an average of **AWB** estimates made over a 60 × 60 m^2 area. The **AWB** estimates were made using empirical equations developed from a subset of destructive **AWB** measurements versus ground spectra and other non-destructive biophysical measurements taken in ten 1 × 1 m^2 quadrats per transect. Ground spectral predictors included aggregated (10 nm bandwidth) HNBs collected with a spectroradiometer. Non-spectral predictors included crop height, the fraction of photosynthetically active radiation absorbed by the canopy (F_{APAR}) estimated with a hand-held ceptometer, and indices derived from Red–Blue–Green (RGB) photo digital numbers. The empirical models of destructive versus non-destructive **AWB** were made using the following predictors, because they had the highest correlation, as defined by the coefficient of determination (R^2), and lowest error, as defined by Root Mean Squared Error (RMSE) in Marshall and Thenkabail, 2015: (1) crop height and HNBs in the NIR (963 and 993 nm) for rice ($R^2 = 0.84$, RMSE = 1.37 g m^{-2}); (2) chromatic greenness (Sonnentag et al., 2012) and HNBs in the visible (428, 468, and 631 nm) for alfalfa ($R^2 = 0.86$, RMSE = 1.81 g m^{-2}); crop height and HNBs in the visible and NIR (539, 560, 943, and 963 nm) for cotton ($R^2 = 0.91$, RMSE = 1.56 g m^{-2}); and crop height, F_{APAR}, and HNBs in the NIR (794, 845, and 865 nm) for maize ($R^2 = 0.59$, RMSE = 1.27 g m^{-2}). Hyperspectral narrowband data are labelled by the median wavelength here and for the remainder of the paper. Summary statistics of **AWB** samples by crop type for transects in 2012 are shown in Table 1. In general, the samples were evenly distributed across the sprouting and flowering/silking stages and less so during the grain/boll-filling stages.

Table 1

Summary statistics (μ = mean and σ = standard deviation) of alfalfa, cotton, maize, and rice **AWB** samples developed from transects in 2012 to build remote sensing models. Statistics are discretized by major phenological stage.

Crop	N	Stage	μ (g m^{-2})	σ (g m^{-2})
Alfalfa	30	Sprouting	1303	937
	31	Flowering/silking	6373	2619
	0	Grain/bud-filling	N/A	N/A
Cotton	30	Sprouting	1088	556
	30	Flowering/silking	7168	2547
	1	Grain/bud-filling	6245	N/A
Maize	29	Sprouting	4107	1147
	17	Flowering/silking	10,181	1297
	15	Grain/bud-filling	14,046	1325
Rice	30	Sprouting	1018	585
	30	Flowering/silking	3080	855
	2	Grain/bud-filling	3400	1677

3.2. Remote sensing imagery and processing

3.2.1. Dataset

We acquired spectral data from the following sensors for analysis: one coarse spatial resolution (MODIS), one medium spatial resolution (Landsat ETM+), three high spatial resolution (IKONOS, GeoEye-1, and WorldView-2), and one hyperspectral (Hyperion). Only the non-thermal and non-panchromatic bands were used. The spectral, spatial, and radiometric characteristics of MODIS, Landsat ETM+ (hereafter Landsat), IKONOS, GeoEye-1 (hereafter GeoEye), WorldView-2 (hereafter WorldView), and Hyperion imagery are presented in Table 2. A total of nine Landsat, 23 IKONOS, 23 GeoEye, 24 WorldView, and ten Hyperion images were used in the analysis. MODIS images were not used directly. Instead, 8-day surface reflectance, captured onboard the Aqua satellite (MYD09A1), were subset for pixels corresponding to the **AWB** transects and downloaded using the Oak Ridge National Laboratory Distributed Active Archive Center for Biogeochemical Dynamic's MODIS Global sub-setting and visualization tool (http://daac.ornl.gov/MODIS/MODIS-menu/modis_webservice.html/). Hyperion imagery in its native format consists of 242 spectral bands, but we only used the 155 bands that were radiometrically calibrated (Simon, 2006) and free from atmospheric contamination or other noise (Thenkabail et al., 2004).

In Table 3, we show the dates ground-based **AWB** measurements were collected and Landsat images were acquired. Given the large number of images used, we omitted this information for the other sensors. We confined remote sensing data to a ±15 day window around the dates the **AWB** measurements were collected. This window was considered conservative, as the acclimation time of temperate croplands to light and temperature has been estimated to be up to ±21 days (Tu, 2000). Landsat ETM+ images were downloaded using the US Geological Survey (USGS) Earth Explorer (http://earthexplorer.usgs.gov/). The high resolution imagery (IKONOS, GeoEye, WorldView) was provided freely through a contractual agreement between the USGS and National Geospatial Intelligence Agency. The reflectance data were accompanied by quality assessment codes. Less than ideal quality measurements (cloud and other noises such as cloud shadow and aerosals) were flagged as missing and filled by linear interpolation. Further inconsistencies were smoothed with a Savitsky–Golay local polynomial filter in the "signal" package in R (http://cran.r-project.org/). The filter was pre-defined as a 3rd-order polynomial with a temporal window of 17 (~136 days).

3.2.2. Image rectification

The images and **AWB** transects were registered as Universal Transverse Mercator 10 north (Datum = WGS 1984). The imagery

Table 2

Sensor characteristics of MODIS (**MD**), Landsat (**LS**), IKONOS (**IK**), GeoEye (**GE**), WorldView (**WV**), and Hyperion (**HY**) imagery. Panchromatic and thermal bands are not included.

Spectral bands	# of Bands	Band range (nm)	Spatial resolution (m)	Digitization (bits)
MD				
1	6	620–670	500	12
2		841–876		
3		459–479		
4		545–565		
5		1230–1250		
7		2105–2155		
LS				
1	6	450–515	30	8
2		525–605		
3		630–690		
4		750–900		
5		1550–1750		
7		2090–2350		
IK				
1	4	445–516	4	11
2		506–595		
3		632–698		
4		757–853		
GE				
1	4	450–510	1.65	11
2		510–580		
3		655–690		
4		780–920		
WV				
1	8	400–450	1.85	11
2		450–510		
3		510–580		
4		585–625		
5		630–690		
6		705–745		
7		770–895		
8		860–900		
HY				
8–57	155	427–925	30	12
79 and 83		933 and 973		
84–119		983–1336		
133		1477		
133–164		1488–1790		
183–184		1982 and 1992		
188–220		2032–2355		

was visually inspected against a vector file of primary and secondary roads from the U.S. Census Bureau's Master Address File/Topologically Integrated Geographic Encoding and Referencing (MAF/TIGER) Database (http://catalog.data.gov/). With the exception of Hyperion, the images showed a high level of geo-location accuracy. For Hyperion, road and field pixels consistently fell outside the road network and transect boundaries, respectively. Therefore, we geometrically corrected the Hyperion images by identifying points at major intersections in the road network vector file as ground control input to the ERDAS IMAGINE® geometric correction routine, specifying a 3rd-order polynomial with nearest neighbor resampling, producing a root mean square error <1 pixel/30 m.

3.2.3. Normalization

Three normalization procedures were performed in order to account for the differences in the radiometric, spatial, and spectral resolutions of each sensor. With the exception of MODIS, which were provided as surface reflectance (%), pixels were expressed as digital numbers (DNs) and were converted to surface reflectance to normalize the data across radiometric resolutions. In order to convert DNs to surface reflectance, images were first converted

Table 3
Landsat (path/row = 44, 33 and 42, 35) and aboveground wet biomass (**AWB**) retrieval dates by crop type. The temporal difference between remote sensing dates and field dates (Δ**T**) did not exceed ±15 days.

Crop	Path	Row	Acquisition date	**AWB** retrieval date	Δ**T**
Alfalfa	42	35	June 10, 2012	June 13, 2012	3
	42	35	June 26, 2012	June 21, 2012	5
	42	35	June 26, 2012	June 19, 2012	7
	44	33	July 10, 2012	July 6, 2012	4
	42	35	July 28, 2012	July 27, 2012	1
	42	35	July 28, 2012	July 28, 2012	0
	42	35	July 28, 2012	August 1, 2012	4
	44	33	August 27, 2012	August 21, 2012	6
	42	35	September 14, 2012	September 17, 2012	3
	44	33	September 12, 2012	September 14, 2012	2
Cotton	42	35	June 10, 2012	June 14, 2012	4
	42	35	June 10, 2012	June 13, 2012	3
	42	35	June 26, 2012	June 19, 2012	7
	42	35	July 28, 2012	July 27, 2012	1
	42	35	July 28, 2012	August 1, 2012	4
	42	35	August 13, 2012	August 7, 2012	6
	42	35	September 14, 2012	September 17, 2012	3
Maize	44	33	July 10, 2012	June 25, 2012	15
	44	33	July 10, 2012	July 2, 2012	8
	44	33	July 10, 2012	July 6, 2012	4
	44	33	August 11, 2012	August 9, 2012	2
	44	33	August 27, 2012	August 21, 2012	6
	44	33	August 27, 2012	August 22, 2012	5
	44	33	September 12, 2012	September 12, 2012	0
	44	33	September 12, 2012	September 14, 2012	2
Rice	44	33	July 10, 2012	June 30, 2012	10
	44	33	July 10, 2012	June 27, 2012	13
	44	33	July 10, 2012	July 6, 2012	4
	44	33	August 11, 2012	August 14, 2012	3
	44	33	August 11, 2012	August 16, 2012	5
	44	33	August 27, 2012	August 24, 2012	3
	44	33	September 12, 2012	September 13, 2012	1
	44	33	September 12, 2012	September 15, 2012	3

to absolute at-sensor radiance (W m^{-2} sr^{-1} μm^{-1}) using standard scaling factors for each sensor band provided in the accompanying metadata. Absolute radiance was then converted to surface reflectance using the Fast Line-of-sight Atmospheric Analysis of Spectral Hypercubes (FLAASH) atmospheric correction algorithm in ENVI®.

Finally, we averaged the surface reflectance of all pixels that fell on an **AWB** transect to produce a single reflectance value for each sensor at each transect, thereby effectively normalizing the spatial resolutions of the images (≈one MODIS pixel, four Landsat and Hyperion pixels, 225 IKONOS pixels, 1322 GeoEye pixels, and 1063 WorldView pixels per transect).

Following Thenkabail (2004), a cross-correlation matrix and accompanying scatterplots (not shown) were generated between each visible and NIR MSBBs to identify major differences in spectral resolution. The strength and direction of each relationship below are expressed with R^2 to reflect the strength of each relationship. Overall, each sensor showed the highest correlations with one another in the NIR (average R^2 across sensors: MODIS = 0.45, Landsat = 0.44, IKONOS = 0.58, GeoEye = 0.56, and WorldView = 0.49) and the lowest correlations with one another in the visible blue (average R^2: MODIS = 0.23, Landsat = 0.23, IKONOS = 0.09, GeoEye = 0.21, and WorldView = 0.08), with visible green and red in between. The strength of the relationships between bands was stronger for the higher spatial resolution MSBB sensors (>0.6), with the strongest being between GeoEye and with IKONOS NIR (R^2 = 0.71). The spatial and spectral properties of MODIS and Landsat were notably different from these sensors, which may contribute to their lower correlations. The low correlations in the visible blue bands was likely due to the sensitivity of this spectral range to atmospheric noise, which was accentuated by the different days and atmospheric conditions under which each sensor

captured reflectance for a given **AWB** estimate. The only two MSBBs that capture reflectance in the SWIR1 and SWIR2 were Landsat and MODIS. The relationship between the two in the SWIR1 was weak (R^2 = 0.08) and moderate in the SWIR2 (R^2 = 0.37). The weak relationship in SWIR1 was likely due to the narrow bandwidth of MODIS that falls within the range of Landsat, whereas the overlap in SWIR2 is placed more comparably.

3.3. Model-building

Given the large number of spectral bands involved and sample area, we built relationships between **AWB** and MSBBs and HNBs using standard empirical data mining techniques (band-ratioing and stepwise linear regression). For the remainder of the paper, these techniques will be referred to as Two-Band Vegetation Indices (TBVIs) and Multiple-Band Vegetation Indices (MBVIs), respectively. Before deriving these indices, the HNBs were first-derivative transformed, which enhanced the vegetation signal by minimizing the impact of soil and other background on each spectrum (Thorp et al., 2004). This step is particularly important in the absence of transmissivity data. The first-derivative transformation was performed on functions fitted to each spectrum using cubic splines with the "stats" package in R. Aboveground wet biomass was transformed logarithmically to facilitate linear model-building. Because the sample sizes varied across sensors, the analysis was performed at three levels of sensor aggregation: each individual MSBB and HNB sensor, all MSBBs, and all sensors combined (MSBBs and HNBs). Because the strength of **AWB** relationships varied between crops, and due the difficulties in retrieving ground spectra for maize **AWB** transects (see Marshall and Thenkabail, 2015), the analysis was also performed for three levels of crop aggregation as well: each crop, all crops (maize omitted), and all crops (maize included).

3.3.1. Band-ratioing: Two-Band Vegetation Index (TBVI)

Two-Band Vegetation Indices were developed by selecting two bands and combining them as in the NDVI formula (Tucker, 1979):

$$\text{TBVI} = \frac{\lambda_2 - \lambda_1}{\lambda_1 + \lambda_2} \qquad (1)$$

where λ_1 is the reflectance for a given MSBB or HNB and λ_2 is the reflectance for a given MSBB or HNB. We derived a TBVI for all possible combinations of λ_1 and λ_2, and tested each index by calculating a linear regression between it and the log-transformed **AWB** across all transect groupings (entire set as well as crop-specific sets). To identify the best TBVIs, the R^2 of the linear regression for every TBVI were plotted in a lambda–lambda (λ–λ) plot (Thenkabail et al., 2000), where the vertical axis is the wavelength centers of λ_1 and the horizontal axis is the wavelength centers of λ_2. In these plots, the best TBVIs were readily identified as "bull-eyes" of high R^2 values. The λ–λ plots were generated for each sensor grouping and each transect grouping to highlight and identify all important band combinations. For each sensor grouping and each transect grouping, the single TBVI with the highest R^2 was chosen for model validation. We also identified all the TBVIs strongly correlated with **AWB**, setting a threshold of R^2 = 0.50, and plotted histograms (frequency of occurrence) of the bands composing these TBVIs to see how well the HNBs performed over all. The statistical analysis was performed in R, while the λ–λ plots were generated with the "ggplot" package in R.

3.3.2. Data reduction: Singular Value Decomposition (SVD)

Multiple-Band Vegetation Indices were developed using the "regsubsets" function in the "leaps" package in R. The regsubsets function takes a stepwise-approach, instead of a forward

addition-approach to model-building, so the number of predictors (**p**) must be less than the number of samples (**N**). Singular Value Decomposition (SVD) (Bretherton et al., 1992), therefore, was performed before the stepwise analysis, so that **p < N**. Singular value decomposition is a common data reduction technique used in image processing and compression to reduce multicollinearity and yield factors (linear combinations) of input variables that explain unique proportions of the input variance (Richards, 2013). Singular value decomposition decomposes a $\mathbf{p} \times \mathbf{N}$ matrix **F** into the form:

$$\mathbf{F} = \mathbf{U}\mathbf{\Gamma}\mathbf{V}^T \tag{2}$$

where **U** is a $\mathbf{p} \times \mathbf{p}$ orthonormal matrix, **V** is an $\mathbf{N} \times \mathbf{N}$ orthonormal matrix, and **Γ** is a diagonal matrix where the number of elements is less than the smaller of **p** or **N**. In our case, **F** consisted of 155 predictor HNBs and 36 (alfalfa), 20 (cotton), 20 (maize), 20 (rice), and 96 (pooled) **AWB** samples. The dimensions of the left singular vectors (**U**) equaled the number of predictor HNBs and of the right singular vectors (**V**) equaled the number of **AWB** samples. The decomposition therefore yielded **N** linear combinations whose loadings described the relative strength of the predictors on each component. Since each component explains successively less variance, we only used the first component to identify the most important HNBs for MBVI development. The SVD was performed using the "SVD" function in R.

3.3.3. Stepwise linear regression: Multiple-Band Vegetation Index (MBVI)

The "regsubsets" function in R was used to perform the stepwise regression, which identifies an optimal set of MSBBs or HNBs combines additively to explain the most predicted variance:

$$MBVI = \mathbf{C_0} + \sum_{i=1}^{nmax} \mathbf{C_i}\mathbf{X_i} \tag{3}$$

where $\mathbf{C_0}$ is the model intercept, **C** is the weighting coefficient of predictor **i**, **X** is the MSBB or HNB predictor, and **nmax** is the maximum number of predictor variables. Regsubsets performs a stepwise search for the linear model that explains the most variance, while minimizing the Bayesian Information Criterion. The Bayesian Information Criterion is used to prevent model over-fitting (Hair et al., 1998). Even so, over-fitting can still occur, so an additional criterion was used: **nmax** was set, so that the ratio of the number of MSBBs or HNBs to the number of **AWB** samples was less than or equal to 0.1. The ratio is typically set between 0.1 and 0.2, where 0.1 is more restrictive than 0.2 (Thenkabail et al., 2000). Unlike other stepwise procedures, the regsubsets function produces a predetermined number of optimal MBVIs up to **nmax** in a convenient tabular format. In our case, we only selected the best MBVI involving up to **nmax** predictors for comparison.

3.3.4. Accuracy assessment

The TBVIs and MBVIs were evaluated visually and numerically. Studentized residual plots (not shown) and scatterplots were used to identify outliers and verify that the assumptions of linear regression were met. Standard model comparison statistics from linear model building (R^2 and RMSE) were computed to evaluate the strength and the sample standard deviation of the differences between observed **AWB** and predicted **AWB**. Since the sample size was small, we expected that the sensitivity of RMSE to the training and validation subsets in a standard split-sample approach would be high (Michaelsen, 1987). We therefore performed a k-fold cross-validation to estimate RMSE, where k is the number of times the subsetting is performed. We set $k = 10$, meaning subsetting was performed ten times, as opposed to $k = \mathbf{N}$ (i.e. leave-one-out cross validation), because the estimate of RMSE from a 10-fold cross

validation is more stable, making it better for model comparison (Arlot and Celisse, 2010).

4. Results

4.1. Band-ratioing: Two-Band Vegetation Index (TBVI)

On a per sensor basis, the **AWB** models using TBVIs derived from high spatial resolution MSBBs performed better than the models using TBVIs derived from coarse (MODIS) or medium (Landsat) spatial resolution MSBBs (Table 4). Table 4 is organized by sensor and crop type. The all crops (maize omitted) aggregation is not displayed, because the results did not significantly differ from the all crops (maize included) aggregation. In all cases, the order in which the two bands are presented represents their order in the TBVI equation (Eq. (1)), with the first band λ_1 and the second λ_2. Of the MSBBs, GeoEye and IKONOS bands 2 and 4 TBVIs (i.e., λ_1 = band 2 and λ_2 = band 4) showed the highest correlations and lowest error when the crops were pooled. When a TBVI involved IKONOS and GeoEye band 4, results were very similar, reflecting the strong correlation between high resolution NIR bands. For individual crops, WorldView bands 6 and 8, GeoEye bands 1 and 4,

Table 4

Summary of the highest ranked TBVIs by crop type for each MSSB and HNB sensor (**MD** = MODIS, **LS** = Landsat, **IK** = IKONOS, **GE** = GeoEye-1, **WV** = WorldView-2, and **HY** = Hyperion). Statistics were determined from the linear regression of log transformed aboveground wet biomass: **N** is the number of samples; λ_1 and λ_2 are the two most significant bands (predictors); and m, b, p, R^2, and RMSE are the slope, intercept, significance, coefficient of determination, and root mean squared error, respectively. The results are significant to the 95% confidence band ($p = 0.05$).

Crop type	N	λ_1	λ_2	m	b	p	R^2	RMSE (g m^{-2})
MD								
Rice	62	2	4	−7.30	5.85	<0.001	0.62	1.63
Alfalfa	59	1	2	8.30	6.59	<0.001	0.59	2.05
Cotton	61	2	4	−9.09	6.16	<0.001	0.59	2.06
Maize	61	1	7	−3.05	13.48	0.007	0.12	1.79
All Crops	243	2	4	−7.04	7.16	<0.001	0.32	2.40
LS								
Rice	56	4	7	−13.07	1.16	<0.001	0.74	1.50
Alfalfa	53	1	5	24.18	−4.64	<0.001	0.53	2.10
Cotton	51	5	7	−9.12	8.75	<0.001	0.58	2.05
Maize	60	3	7	−6.58	14.37	<0.001	0.59	1.50
All Crops	220	5	7	−7.35	8.99	<0.001	0.25	2.47
IK								
Rice	52	2	4	4.50	7.88	<0.001	0.79	1.48
Alfalfa	59	2	3	−14.46	12.07	<0.001	0.62	2.02
Cotton	61	3	4	6.75	7.43	<0.001	0.93	1.35
Maize	61	1	2	−7.79	15.22	<0.001	0.63	1.45
All Crops	233	2	4	6.09	7.63	<0.001	0.53	2.10
GE								
Rice	52	2	4	3.84	8.06	<0.001	0.69	1.60
Alfalfa	59	1	4	11.70	2.05	<0.001	0.73	1.81
Cotton	61	3	4	7.15	6.68	<0.001	0.92	1.35
Maize	61	1	4	3.67	9.44	<0.001	0.22	1.72
All Crops	233	2	4	6.38	7.15	<0.001	0.57	2.04
WV								
Rice	62	6	8	5.52	9.33	<0.001	0.85	1.36
Alfalfa	49	3	4	−9.72	11.00	<0.001	0.33	2.46
Cotton	51	4	7	7.28	7.41	<0.001	0.66	1.94
Maize	61	2	4	4.95	11.70	<0.001	0.40	1.60
All Crops	223	6	7	7.90	9.45	<0.001	0.42	2.27
HY								
Rice	20	549	752	1.82	9.62	<0.001	0.91	1.22
Alfalfa	36	925	1104	−0.95	12.34	<0.001	0.81	1.73
Cotton	20	722	732	11.18	12.51	<0.001	0.97	1.26
Maize	20	529	895	−0.66	13.05	<0.001	0.94	1.15
All Crops	96	539	752	3.85	9.34	<0.001	0.56	2.19

IKONOS bands 3 and 4, and IKONOS bands 1 and 2 were the top performers for rice, alfalfa, cotton, and maize, respectively.

The λ–λ plot for all HNB combinations are shown on a per crop basis in Fig. 2, while the histograms in Fig. 3 illustrate the most frequent bands included in the highest ranked HNB TBVIs. Cotton and maize **AWB** tended to be correlated with a wider range of HNBs than rice or alfalfa **AWB**. The highest and most frequently correlated TBVIs for cotton included bands that were centered at three important HNBs: NIR, SWIR1, and SWIR2 (732, 1124, and 1982 nm). The model for maize also highlighted HNB band 732 nm as a band commonly included in the highest and most frequently correlated TBVIs. In addition, strong correlations of **AWB** models for maize resulted in TBVIs that included HNB NIR (854 nm) and bands across a narrow region centered at 1225 nm in the SWIR1. For rice, TBVIs involving three narrow regions centered at 691, 752, and 813 nm in the red-edge NIR tended to be the best performers, mirroring the MSBB results. Alfalfa **AWB** was the least responsive, with the highest and most frequently correlated TBVIs including bands centered at 1104 nm in the SWIR1.

The HNB TBVIs performed as well or better than the MSBB TBVIs (Table 4). Like the best MSBB TBVI, the visible green (539 nm) and NIR (752 nm) bands yielded the highest correlations and lowest error when all crops were included, however, the HNB TBVI explained 1% less variance than the best MSBB TBVI. On an individual crop basis, however, the HNBs did better: for rice, visible green (549 nm) and NIR (752 nm) explained an additional 6% in **AWB** variance than the best MSBB TBVI; for alfalfa, NIR (925 nm) and SWIR1 (1104 nm) explained an additional 8% in **AWB** variance than the best MSBB TBVI; for cotton, NIR (722 and 732 nm) explained an additional 4% in **AWB** variance than the best MSBB TBVI; and for maize, visible green (529 nm) and NIR (895 nm) explained an additional 31% in **AWB** variance than the best MSBB TBVI.

4.2. Stepwise linear regression: Multiple-Band Vegetation Index (MBVI)

The ability of MSBB MBVIs to predict **AWB** was significantly better than the MSBB TBVIs (Table 5). The MODIS MBVI for rice (bands 2 and 4), Landsat MBVI (bands 5 and 7) for alfalfa, GeoEye MBVI (bands 1 and 3) for maize, WorldView MBVI (bands 2 and 4) for alfalfa, and WorldView MBVI (bands 7 and 8) for maize, explained an additional 25%, 29%, 37%, 24%, and 20% of **AWB** variance, respectively. On a per crop basis, however, models of **AWB** developed from stepwise linear regression were more mixed and less consistent than models developed using MSBB TBVIs. This was true for all high, medium, and coarse spatial resolution MSBB MBVIs. Note that we distinguish the optimal MBVIs
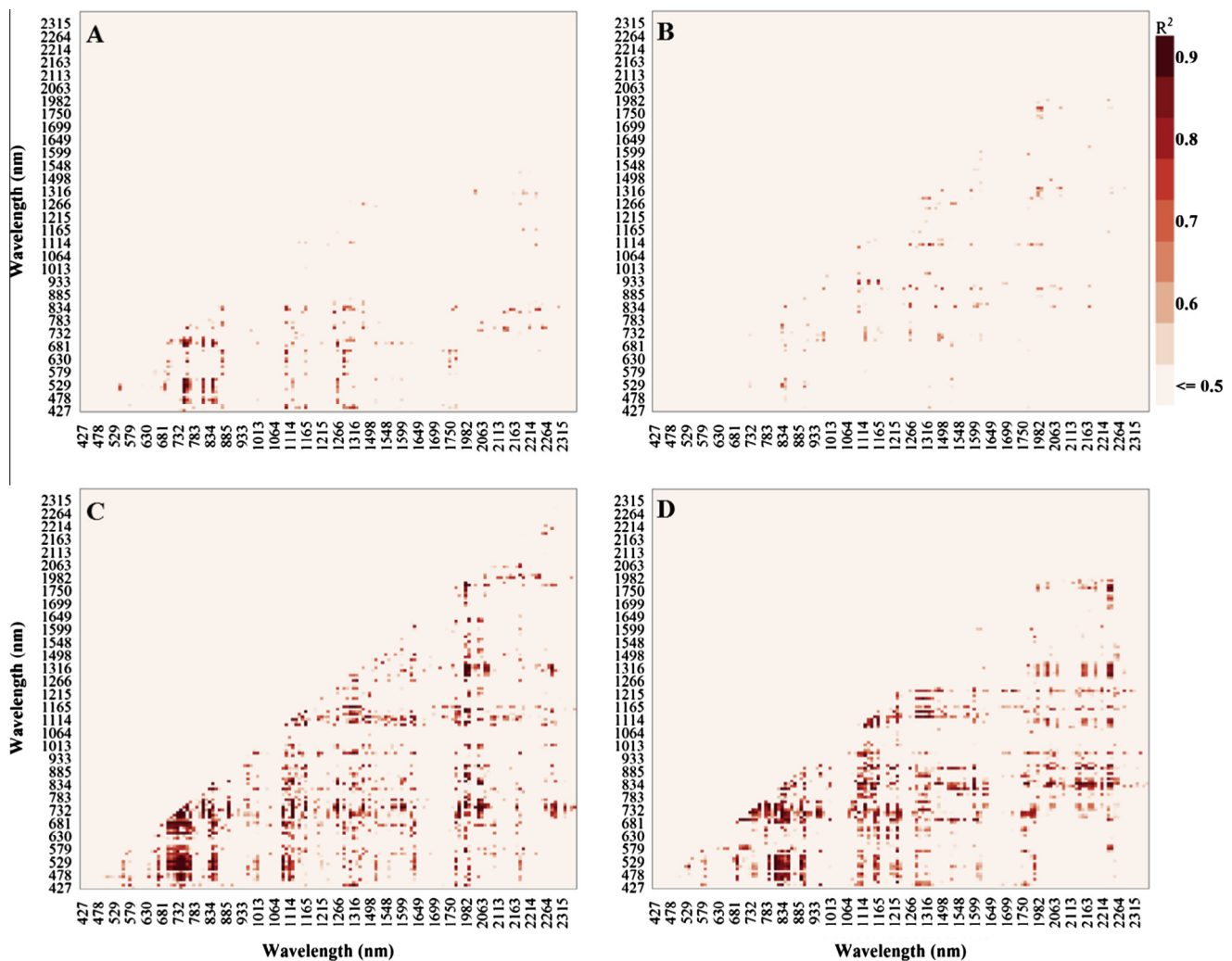
Fig. 2. Lambda–lambda (coefficient of determination-R^2) contour plots created from 155 first-derivative transformed hyperspectral narrowbands and rice (A), alfalfa (B), cotton (C), and maize (D) aboveground wet biomass. The number of samples used to develop the statistics was 20, 36, 20, and 20, respectively. Two-band vegetation indices with R^2 less than or equal to 0.5 were masked to accentuate relatively strong relationships.
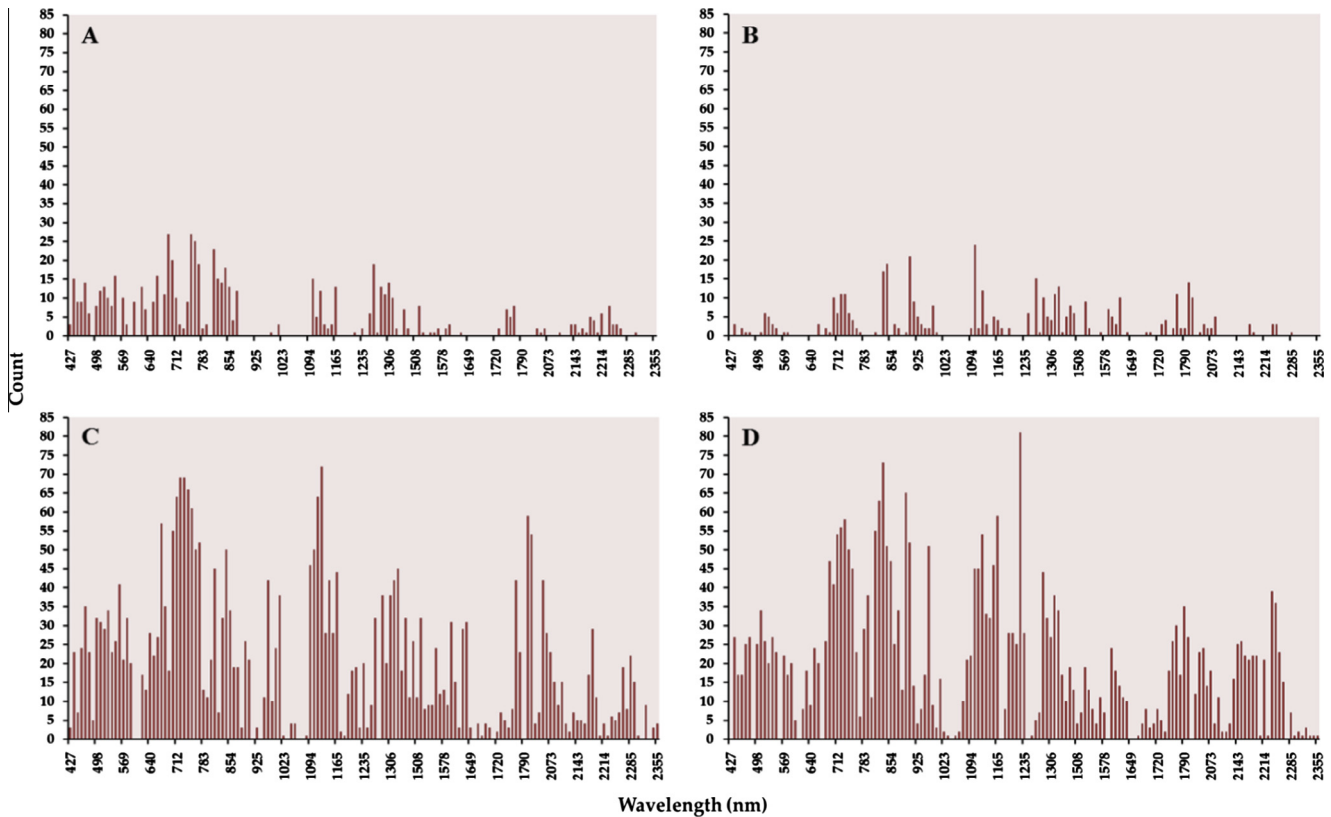
Fig. 3. Histograms showing the frequency of occurrence of hyperspectral narrowbands in two-band vegetation indices with correlation of determination greater than 0.5 for rice (A), alfalfa (B), cotton (C), and maize (D) aboveground wet biomass.

using two bands to be consistent with MSBB TBVIs; these are the two bands that display the highest loadings in the MBVI models.

For all crops pooled, GeoEye bands 2 and 4 yielded the highest correlation and lowest RMSE of the MSBBs, mirroring the TBVI analysis. For rice, MODIS bands 2 and 4 performed on par with IKONOS (bands 2 and 4), GeoEye (bands 2 and 4), and WorldView (bands 7 and 8). For alfalfa, Landsat bands 5 and 7 outperformed IKONOS (bands 3 and 4), GeoEye (bands 1 and 4), and WorldView (bands 2 and 4). For cotton, as found in the TBVI analysis, GeoEye and IKONOS bands 3 and 4 performed considerably better than MODIS and Landsat. MODIS bands performed poorly with maize **AWB**, while results for GeoEye (bands 1 and 3), IKONOS (bands 3 and 4), and WorldView (bands 7 and 8) were comparable to TBVI results. With the exception of a dozen cases out of the 25 MBVIs listed in Table 5, the incorporation of more MSBBs into the MBVIs either increased the RMSE and/or did not significantly add to explained **AWB** variance ($\Delta R^2 \leqslant 0.02$).

The ability of HNB MBVIs to predict **AWB** was mildly better than the HNB TBVIs (Table 5). For all crops, the model using the HNB MBVI that involved two NIR bands (813 and 1114 nm) explained an additional 15% of **AWB** variance compared to the HNB TBVI. As with the TBVIs, HNB MBVIs out-performed MSBB MBVIs in all cases. The best MSBB MBVI for rice (IKONOS bands 2 and 4) explained 3% lower **AWB** variance than the best HBN MBVI. The best MSBB MBVI for alfalfa (Landsat bands 5 and 7) explained 4% lower **AWB** variance than the best HBN MBVI. The best MSBB MBVI for cotton (GeoEye bands 3 and 4) explained 3% lower **AWB** variance than the best HBN MBVI. The best MSBB MBVI for maize (**GE** bands 1 and 3 and WorldView bands 7 and 8) explained 33% lower **AWB** variance than the best HBN MBVI – a difference considerably larger than any other crop. Other important HNBs (derived from the SVD analysis) are shown in Table 6.

For convenience, only the top 19 HNBs by component loading identified in the SVD and used to constrain the stepwise regression are shown. We only used HNBs from the first component, because they explained 84%, 78%, 89%, and 72% of the HNB variability, while the second components explained only an additional 6%, 8%, 3%, and 10% of the HNB variability for rice, alfalfa, cotton, maize, and all crops, respectively. The HNBs were primarily in the NIR and secondly in the SWIR1. Cotton included one HNB in the SWIR2 (1982 nm).

4.3. Two-Band Vegetation Indices (TBVIs) and Multiple-Band Vegetation Indices (MBVIs) across sensors

We explored the possibility that **AWB** models could be improved by combining reflectance data from two different sensors to calculate TBVIs and MBVIs. The merging of MSBBs and HNBs into vegetation indices led to erratic responses (not shown), due to small sample sizes and over-fitting, so we only present the results of merging MSBBs here. Fig. 4 shows λ–λ plots for each crop, indicating the most highly correlated TBVIs across MSBBs. Rice and cotton showed the highest correlations across the MSBBs, and less so for alfalfa and maize. For rice, the combination of WorldView (bands 7 and 8) across MSBBs yielded high correlations with **AWB**, while IKONOS (band 4) was more robust, but yielded relatively lower correlations. Although alfalfa and maize showed lower correlations over a narrower range of sensors, merging MSBB TBVIs for these two crops yielded higher correlations than with individual sensors. The combination of GeoEye (band 2) and Landsat (band 4) for alfalfa ($R^2 = 0.77$, RMSE = 1.36 g m^{-2}) led to a 4% increase in explained variance over the best individual MSBB TBVI, while the combination of IKONOS (band 1) and GeoEye (band 2) for maize ($R^2 = 0.80$, RMSE = 1.31 g m^{-2}) led to a 17%

Table 5
Summary of the highest ranked multiple-band vegetation indices by crop type for each MSSB and HNB sensor (**MD** = MODIS, **LS** = Landsat, **IK** = IKONOS, **GE** = GeoEye-1, **WV** = WorldView-2, and **HY** = Hyperion). Statistics were determined from the linear regression of log transformed aboveground wet biomass: N is the number of samples; λ_1 and λ_2 are the two most significant bands (predictors); and m, b, p, R^2, and RMSE are the slope, intercept, significance, coefficient of determination, and root mean squared error, respectively. The results are significant to at least the 95% confidence band ($p = 0.05$).

Crop type	N	λ_1	λ_2	m_1	m_2	b	p_1	p_2	R^2	RMSE (g m^{-2})
MD										
Rice	62	2	4	10.37	8.72	6.63	<0.001	0.045	0.88	1.32
Alfalfa	59	1	2	−24.59	8.12	10.75	<0.001	<0.001	0.61	2.04
Cotton	61	2	4	10.40	−19.82	9.31	<0.001	0.008	0.58	2.08
Maize	61	2	5	−3.89	9.55	11.08	0.055	0.015	0.10	1.82
All Crops	243	2	4	9.39	−12.40	9.06	<0.001	<0.001	0.37	2.35
LS										
Rice	56	4	7	11.79	−52.47	9.23	<0.001	<0.001	0.76	1.46
Alfalfa	53	5	7	87.73	−104.61	3.16	<0.001	<0.001	0.82	1.61
Cotton	51	3	7	35.73	−47.40	14.25	<0.001	<0.001	0.65	1.99
Maize	60	3	7	60.40	−37.73	12.79	<0.001	<0.001	0.53	1.58
All Crops	220	5	7	28.52	−41.09	10.23	<0.001	<0.001	0.32	2.36
IK										
Rice	52	2	4	−9.97	6.55	8.99	0.021	<0.001	0.89	1.35
Alfalfa	59	3	4	−8.81	8.84	8.66	0.003	<0.001	0.62	2.03
Cotton	61	3	4	−16.53	10.39	9.15	<0.001	<0.001	0.94	1.34
Maize	61	3	4	22.97	3.34	10.08	<0.001	<0.001	0.58	1.52
All Crops	233	3	4	−10.26	7.11	9.72	<0.001	<0.001	0.50	2.17
GE										
Rice	52	2	4	−4.85	6.90	8.48	<0.001	<0.001	0.88	1.36
Alfalfa	59	1	4	−41.74	4.38	11.37	<0.001	<0.001	0.75	1.79
Cotton	61	3	4	−17.46	6.30	10.05	<0.001	<0.001	0.95	1.29
Maize	61	1	3	−81.13	48.13	12.46	<0.001	<0.001	0.60	1.52
All Crops	233	2	4	−19.73	5.60	10.64	<0.001	<0.001	0.55	2.08
WV										
Rice	62	7	8	8.36	−5.00	11.57	<0.001	<0.001	0.87	1.33
Alfalfa	49	2	4	59.00	−50.21	12.53	<0.001	<0.001	0.57	2.18
Cotton	51	2	5	33.61	−42.80	13.40	<0.001	<0.001	0.83	1.60
Maize	61	7	8	−40.22	47.28	10.73	<0.001	<0.001	0.60	1.50
All Crops	223	6	7	−12.10	9.23	10.57	<0.001	<0.001	0.36	2.37
HY										
Rice	20	1124	1134	190.49	−216.49	8.96	<0.001	<0.001	0.92	1.61
Alfalfa	36	834	1114	−1502.06	−434.99	11.07	<0.001	<0.001	0.85	1.66
Cotton	20	1114	1982	−133.41	665.86	12.08	0.005	<0.001	0.98	1.23
Maize	20	813	895	809.58	−272.34	13.01	<0.001	0.079	0.93	1.18
All Crops	96	813	1114	1280.11	−402.48	9.48	<0.001	<0.001	0.71	1.91

Table 6
List of the hyperspectral narrowbands (HNBs) that had the highest loadings on the first component of the singular value decomposition. The HNBs are listed in numerical order. The first component explained 84%, 78%, 89%, and 72% of the HNB variability for rice, alfalfa, cotton, maize, and all crops, respectively.

Rice	Alfalfa	Cotton	Maize	All crops
702	732	722	742	732
712	742	732	752	742
722	895	742	763	895
732	905	752	813	905
742	925	905	834	915
752	933	925	895	925
763	973	933	905	933
844	983	973	915	973
905	1094	1094	925	983
925	1104	1114	933	1094
933	1114	1124	973	1104
1104	1124	1134	1094	1114
1124	1134	1155	1104	1124
1134	1144	1165	1114	1134
1144	1155	1306	1134	1144
1165	1165	1336	1144	1155
1306	1316	1488	1155	1165
1316	1326	1498	1165	1316
1326	1336	1982	1326	1326

(band 4) ($R^2 = 0.95$, RMSE = 1.22 g m^{-2}) led to a 7% increase in explained model variance over the individual MSBB MBVI for rice. The combination of IKONOS (band 1) and GeoEye (band 2) for maize ($R^2 = 0.85$, RMSE = 1.27 g m^{-2}) led to a 25% increase in explained variance over the best individual MSBB MBVI.

Scatterplots of predicted **AWB** versus reference **AWB** for the highest correlated MSBB and HNB vegetation index on a per crop basis using either individual or combined sensors are shown in Figs. 5 and 6, respectively. There are fewer data points in Fig. 6 because Hyperion acquisition was much more limited than MSBB acquisition and the spatial extent of Hyperion imagery is much narrower than many of the other MSBB imagery. In each case, the MBVI approach was selected, because it yielded higher correlations and lower error than the TBVI approach. In general, the HNB MBVI residuals appeared almost bimodal, while the MSBB MBVI residuals appeared to be more randomly distributed.

5. Discussion

The study examined the ability of several MSBBs (GeoEye-1, IKONOS, Landsat ETM+, MODIS, and WorldView-2) and HNBs (Hyperion) to estimate **AWB** for four of California's most water-intensive crops (alfalfa, cotton, maize, and rice). The analysis was performed on a per-crop and per-sensor basis, but the ability of combining MSBBs across sensors to simulate **AWB** was also

increase in explained variance over the best individual MSBB TBVI. The MBVI approach, via MSBB merging, yielded modest improvements as well. The combination of MODIS (band 2) and GeoEye
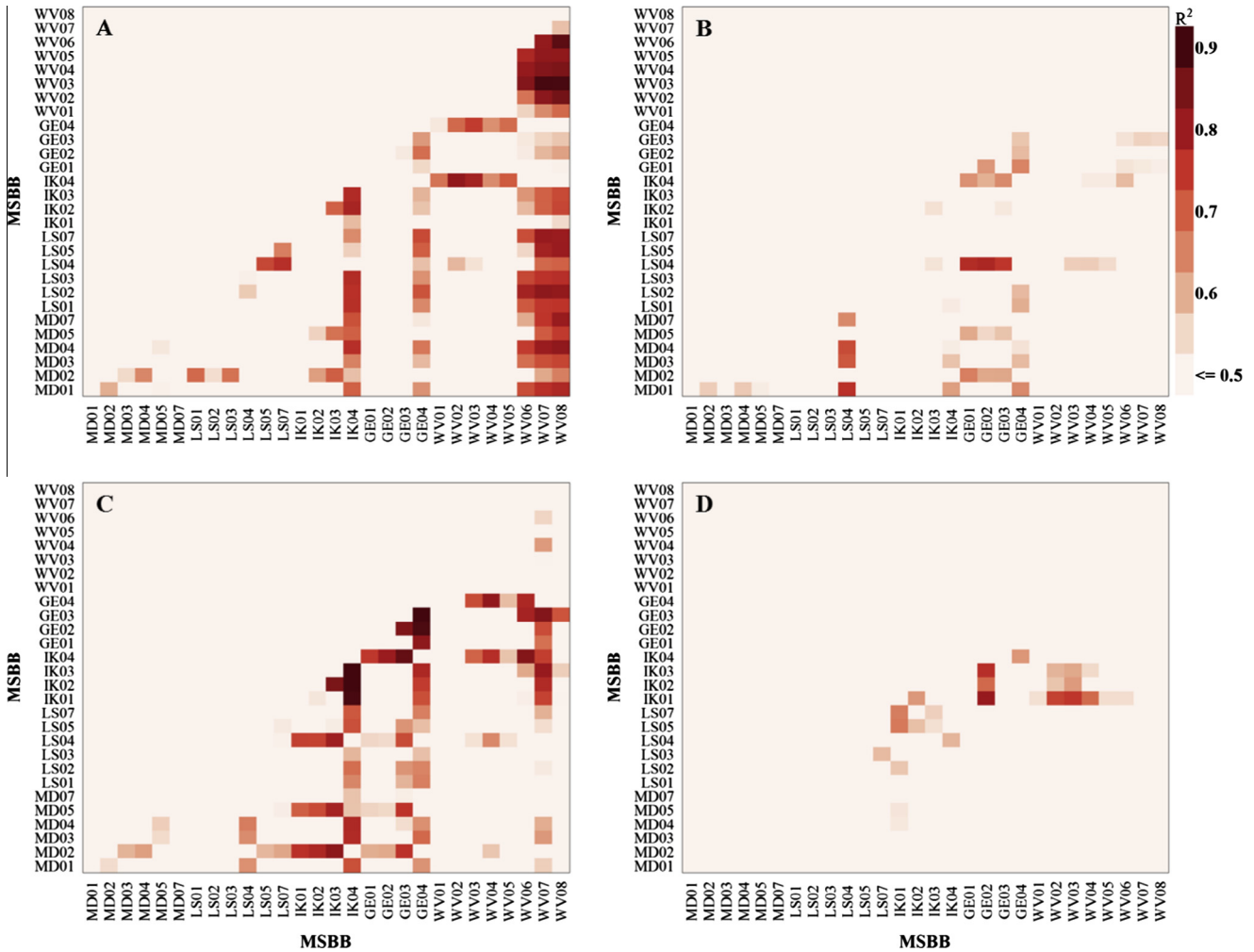
Fig. 4. Lambda–lambda (coefficient of determination-R^2) contour plots created from 28 multispectral broadbands and rice (A), alfalfa (B), cotton (C), and maize (D) **AWB** samples. The number of samples used to develop the statistics was 47, 46, 45, and 60, respectively. Two-band vegetation indices with R^2 less than or equal to 0.5 were masked to accentuate relatively strong relationships.

evaluated. The comparison was done by building linear models that related log-transformed **AWB** with vegetation indices. The vegetation indices combined MSBBs and HNBs either as a normalized ratio (TBVI) or additively (MBVI). The performance of each model was ranked according to its correlation and cross-validation statistics to select a model for comparison.

The highest ranked HNB TBVIs and MBVIs in general, performed better than the highest ranked MSBB TBVIs and MBVIs, indicating that narrow spectral bands are more important than high spatial resolution bands in predicting **AWB**. Narrowband models exploit specific spectral regions sensitive to crop characteristics and reduce redundant or insignificant spectral regions, while broadband models average information over larger spectral regions. Caution should be taken in interpreting these results, however, as the HNB models were built using smaller samples sizes ($N = 20$, 36, 20, and 20 for rice, alfalfa, cotton, and maize, respectively). The small sample sizes led to potential over-fitting and leveraging that was observed in the scatterplots (shown) and residual plots (not shown). We would expect that over-fitting and leveraging would inflate the predictive ability of the models, but this was not reflected in the cross-validation analysis.

The explanatory power of HNB TBVIs ($R^2 = 0.56$) compared to MSBB TBVIs ($R^2 = 0.57$) was negligible, while the gains made using HNB MBVIs ($R^2 = 0.71$) versus MSBB MBVIs ($R^2 = 0.49$) was more

substantial. The two most important HNBs (from the pooled analysis) were in the NIR (813 nm) and SWIR1 (1114 nm) when HNBs were combined using stepwise regression (MBVI), while the visible green (539 nm) became important when HNBs were combined as ratios (TBVI). The two NIR HNBs correspond to strong scattering peaks in and are due to light interaction with plant cell walls (Ollinger, 2011). Alfalfa, which did not have a senescent phase and is a strong planophile, showed the highest correlation with the wavelength where scatter in the NIR due to accumulated biomass is the highest (1104 nm). The green HNB corresponds to the largest scattering peak in the visible range, which is due to the spectral properties of plant chlorophyll and accessory pigments. The results of the per-crop analysis were similar to the pooled analysis, but variations were observed and can be due to any number of differences among crops characterized by: leaf angle geometry, plant physiology, irrigation timing and regime, fertilizer application, and background soil properties. For example, the TBVIs for rice and maize, as in the pooled TBVI, involved visible green wavelengths (549 and 529 nm) and NIR wavelengths (752 and 895 nm) that lie within the same spectral range where chlorophyll/accessory pigments (alignment of plant cell walls) absorb (scatter) light, while the TBVI for cotton involved two wavelengths (722 and 732 nm) that lie outside these ranges in the red-edge. The red-edge tends to shift in response to plant stress (Merton and
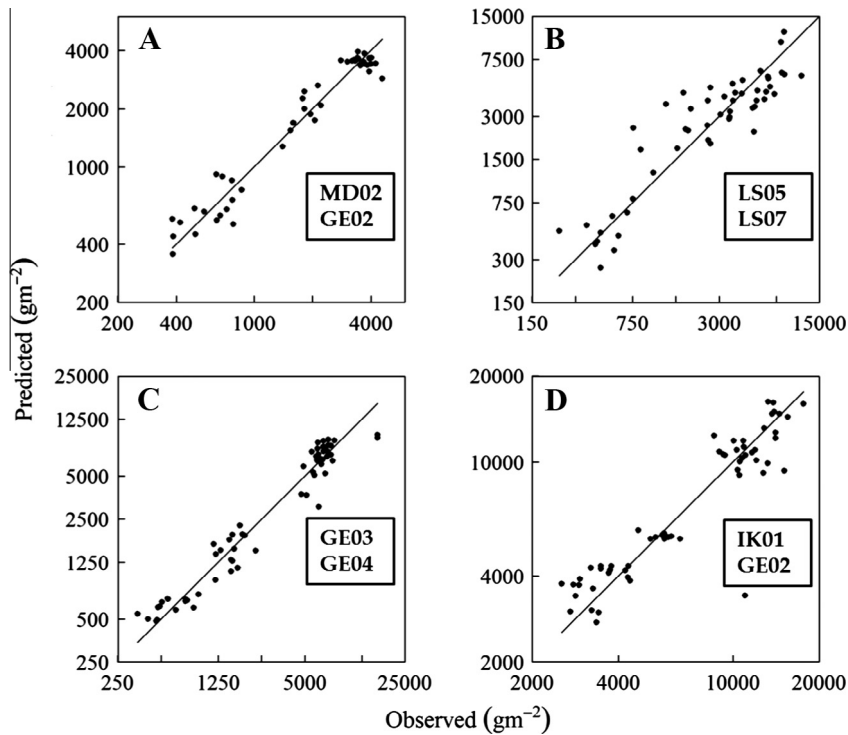
Fig. 5. Scatterplots of predicted versus reference **AWB** for the highest correlated vegetation indices using all possible MSBB combinations for rice (A), alfalfa (B), cotton (C), and maize (D). In each case, the MBVI approach resulted in the highest correlations. The diagonal line represents a 1:1 relationship between predicted and reference **AWB**.
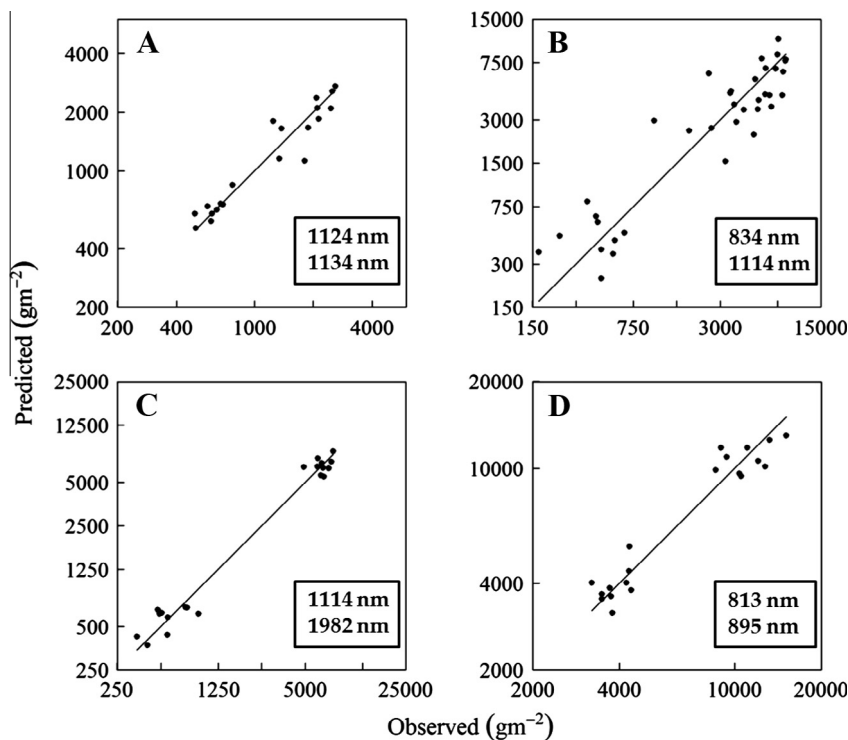
Fig. 6. Scatterplots of predicted versus reference **AWB** for the highest correlated vegetation indices using hyperspectral narrowbands for rice (A), alfalfa (B), cotton (C), and maize (D). In each case, the MBVI approach resulted in the highest correlations. The diagonal line represents a 1:1 relationship between predicted and reference **AWB**.

Huntington, 1999) and could therefore be reflecting the poor soil quality characteristic of cotton fields in the Central Valley and reduction in fertilizer and water application during boll formation that increases harvest efficiency and yields. Similarly, the MBVIs

for each crop involve various strong scattering wavelengths due to the alignment of plant cell walls (813, 834, 895, 1114, 1124, and 1134 nm), while cotton is the only crop that includes a SWIR2 wavelength (1982 nm) in its top performing MBVI. This

wavelength corresponds to a strong water absorption region and could therefore be indicating water status. The SWIR2 region was particularly noisy and could be obscuring its importance in **AWB** estimation for the other crops.

Perhaps the most interesting findings of the analysis lie with the MSBBs. Overall, IKONOS and GeoEye using the green and NIR bands produced the highest correlated TBVIs and MBVIs with **AWB** of the MSBBs, as we might expect, because of their high spatial resolution. In general, the two sensors were highly correlated and could be used interchangeably, but GeoEye had a slight advantage over IKONOS that can be attributed to its higher spatial resolution.

The performance of WorldView, with its relatively high spatial and spectral resolution, was unexpectedly poor for all the crops, except rice. The reflectance from two WorldView images (acquisition dates = July 18, 2012 and August 22, 2012) were averaged for cotton **AWB** transects made on August 7, 2012, because of high demand for the sensor during the Olympic Games in London, United Kingdom. Even so, the cotton transects were not flagged as outliers when inspecting the residuals. In addition, rice, which resulted in high **AWB** and WorldView correlations had image acquisition dates that were the farthest from **AWB** retrieval dates. Three of the WorldView images were the only high resolution images that had noticeable cloud cover and this could have contaminated ground reflectance estimates. It will be interesting to see in future work if the newly deployed WorldView sensor will perform better, with its higher spatial resolution and added spectral bands in the NIR and SWIR.

The most promising results lie with the ability of MODIS and Landsat NIR to predict **AWB**, which yielded high correlations for rice and alfalfa. MODIS has narrower spectral bands than Landsat and previous research has shown (e.g. Marshall and Thenkabail, 2014) that rice is sensitive to a much narrower spectral range than other crops, again reflecting the importance of spectral resolution over spatial resolution. In the future, a comparative analysis between the recently operational Landsat OLI (with its higher spectral resolution than Landsat ETM+) and MODIS could provide more evidence of this hypothesis.

The MBVIs in general, performed better than the TBVIs for MSBBs and HNBs. Based on the pooled analysis, the improvement was greater with the HNB MBVIs ($R^2 = 0.71$ versus $R^2 = 0.56$) than the MSBB MBVIs ($R^2 = 0.55$ versus $R^2 = 0.53$). On a per crop basis, the differences were even more pronounced. This could reflect the modest ability of TBVIs, such as NDVI, to estimate **AWB** at coarse spatial resolution compared to smaller scale and crop-specific targets. If the results presented here were not constrained to two variables, so that a legitimate comparison could be made with TBVIs, the superiority of the MBVI approach was more pronounced. For example, MODIS band 2 alone for rice ($R^2 = 0.87$ and RMSE = 1.34 g m^{-2}); Landsat bands 3, 4, and 7 for cotton ($R^2 = 0.76$ and RMSE = 1.75 g m^{-2}); GeoEye bands 1, 2, and 3 for alfalfa ($R^2 = 0.78$ and RMSE = 1.72 g m^{-2}); IKONOS bands 2, 3, and 4 for maize ($R^2 = 0.63$ and RMSE = 1.51 g m^{-2}); and WorldView bands 2, 7, and 8 for rice ($R^2 = 0.92$ and RMSE = 1.27 g m^{-2}) led to higher correlations and lower errors on a per-sensor basis than the MBVIs using two bands presented here.

The MBVI approach has been criticized, because it is sensitive to over-fitting, does not fully account for multicollinearity, and often fails to produce bands that reflect known absorption features (Grossman et al., 1996). To overcome these obstacles, SVD was used to minimize the effects of multicollinearity and rules were applied to restrict the number of predictors to prevent over-fitting. These factors undoubtedly contributed to the interpretability of the HNBs. Partial least squares regression is perhaps more straight forward than a combined SVD and stepwise approach to build vegetation indices, however a previous analysis using

ground-level spectroradiometric data, showed PLSR type models performed worse than stepwise regression on validation subsets (Marshall and Thenkabail, 2015). Cetin and Musaoglu, 2009 reviewed and compared the most non-parametric approaches to multi-sensor data fusion. These should be evaluated in the future because they are more flexible and less sensitive to outliers than parametric techniques like stepwise regression.

It is difficult to compare the results of this study to others, due to the issue of transferability, the different sample sizes and sampling techniques, and the different processing steps and modeling techniques. Another consideration is the sensitivity of **AWB** to canopy water content, which varies drastically across space and time. This may explain the relatively poor performance of SWIR MSBBs and HNBs, which are also sensitive to canopy water content. To illustrate these difficulties, we compare our findings to Mariotto et al. (2013), who performed an evaluation of MSBBs and HNBs for predicting **AWB** for alfalfa, cotton, maize, rice, and wheat fields in a region with complex topography (Syr Darya river basin in Uzbekistan). As in our study, *in situ* **AWB** data was log-transformed and TBVIs and MBVIs were developed for inter-model comparison. In contrast to our study, the images were not georectified and the HNBs were not first-derivative transformed and no validation was performed. In addition, *in situ* **AWB** was not extrapolated over transects corresponding to the spatial resolution of the sensors analyzed.

The two studies produced results both similar and dissimilar. Like this study, Hyperion HNBs performed better than MSBBs, and MBVIs performed better than TBVIs. Unlike this study, Landsat consistently performed better than IKONOS or Quickbird (another high spatial resolution sensor). For the crops reported, the optimal HNBs for cotton ($R^2 = 0.95$, $N = 16$) and maize ($R^2 = 0.99$, $N = 9$), were in the NIR and SWIR2 (2052 and 2285 nm); and visible blue (427 and 437 nm), NIR (973 nm), and SWIR1 (1165 nm), respectively. This somewhat overlaps with the results of this study, but the sample sizes in the Uzbekistan study tended to be small and the number of predictors large. The combination of small sample size and a large number of predictors is particularly problematic for forward selection automated regression methods (Hair et al., 1998), which was the approach taken to build the MBVIs in that study. For the crops reported, similarities between the two studies involving Landsat were quite divergent. Landsat bands 1, 4, and 6 yielded the highest correlation to cotton **AWB** ($R^2 = 0.55$, $N = 38$), while Landsat bands 1, 6, and 7 yielded the highest correlation to maize **AWB** ($R^2 = 0.62$, $N = 14$) in the Uzbekistan study. In this study, Landsat bands 3, 4, and 7 yielded the highest correlation with cotton **AWB** ($R^2 = 0.76$, $N = 51$) and Landsat bands 4, 5, and 7 yielded the highest correlation with maize **AWB** ($R^2 = 0.60$, $N = 60$). It is difficult to know whether the contrasting results are due to different methodologies or different biophysical settings. Given the potential difficulty, therefore in using the empirically-based models beyond the area they are developed, the models developed here may be best suited to develop larger **AWB** transects to calibrate/validate physically-based agro-ecosystem models.

6. Conclusions

This research compared multispectral broadband (MSBB) data from: three high spatial resolution (sub-meter to 5 m) sensors (IKONOS, GeoEye-1, and WorldView-2); one moderate resolution sensor (Landsat ETM+), and one coarse resolution sensor (MODIS) with hyperspectral narrowband (HNB) data from EO-1 Hyperion in studying aboveground biomass (**AWB**) of four water-intensive crops (alfalfa, cotton, maize, and rice) in the Central Valley of California. The importance of high spectral resolution, as opposed

to high spatial resolution, in quantifying **AWB** is well established in this research: overall, hyperspectral narrowband vegetation indices explained 3–33% greater variability in modeling **AWB** than MSBB vegetation indices. The study also established the importance of the red-edge (700–740 nm), which is absent in most MSBBs, and identified six specific HNBs within the 400–2500 nm range that explained the most **AWB** variability: 539 nm, 722 nm, 758 nm, 914 nm, 1130 nm, 1320 nm (bandwidth of 10 nm). These are the optimal bands with nearby bands often producing similar results. When hyperspectral data are available, such as from narrowly-focused EO-1 Hyperion HNBs, as identified here, significant advances can be made in quantifying and modeling agricultural crop biomass. Most importantly, the HNB vegetation indices can be used to return rapidly, estimates of crop **AWB** over large areas, which in turn can be used to calibrate/validate agroecosystem models at multiple scales.

Acknowledgements

References

Arlot, S., Celisse, A., 2010. A survey of cross-validation procedures for model selection. Statist. Surv. 4, 40–79.

Asner, G.P., 1998. Biophysical and biochemical sources of variability in canopy reflectance. Remote Sens. Environ. 64, 234–253.

Bretherton, C.S., Smith, C., Wallace, J.M., 1992. An intercomparison of methods for finding coupled patterns in climate data. J. Clim. 5, 541–560.

Carter, G.A., 1991. Primary and secondary effects of water content of the spectral reflectance of leaves. Am. J. Bot. 78, 916–924.

Casa, R., Jones, H.G., 2004. Retrieval of crop canopy properties: a comparison between model inversion from hyperspectral data and image classification. Int. J. Remote Sens. 25, 1119–1130.

Cetin, M., Musaoglu, N., 2009. Merging hyperspectral and panchromatic image data: qualitative and quantitative analysis. Int. J. Remote Sens. 7, 1779–1804.

Dettinger, M.D., Cayan, D.R., Meyer, M.K., Jeton, A.E., 2004. Simulated hydrologic responses to climate variations and change in the Merced, Carson, and American River Basins, Sierra Nevada, California, 1900–2099. Climatic Change 62, 283–317.

Dorigo, W.A., Zurita-Milla, R., De Wit, A.J.W., Brazile, J., Singh, R., Schaepman, M.E., 2007. A review on reflective remote sensing and data assimilation techniques for enhanced agroecosystem modeling. Int. J. Appl. Earth Obs. Geoinf. 9, 165–193.

Elvidge, C.D., Chen, Z., 1995. Comparison of broad-band and narrow-band red and near-infrared vegetation indices. Remote Sens. Environ. 54, 38–48.

Houghton, R.A., 2010. How well do we know the flux of CO_2 from land-use change? Tellus B 62, 337–351.

Houghton, R.A., Hall, F., Goetz, S.J., 2009. Importance of biomass in the global carbon cycle. J. Geophys. Res.: Biogeosci. 114 (G2), G00E03.

Gitelson, A.A., Keydan, G.P., Merzlyak, M.N., 2006. Three-band model for noninvasive estimation of chlorophyll, carotenoids, and anthocyanin contents in higher plant leaves. Geophys. Res. Lett. 33, L11402. http://dx.doi.org/10.1029/2006GL026457.

Goetz, A.F.H., 2009. Three decades of hyperspectral remote sensing of the Earth: A personal view. Remote Sens. Environ. 113, S5–S16.

Grossman, Y.L., Ustin, S.L., Jacquemoud, S., Sanderson, E.W., Schmuck, G., Verdebout, J., 1996. Critique of stepwise multiple linear regression for the extraction of leaf biochemistry information from leaf reflectance data. Remote Sens. Environ. 56, 182–193.

Hair Jr., J.F., Anderson, R.E., Tatham, R.L., Black, W.C., 1998. Multivariate Data Analysis, fifth ed. Prentice Hall, Upper Saddle River, NJ.

Hansen, P.M., Schjoerring, J.K., 2003. Reflectance measurement of canopy biomass and nitrogen status in wheat crops using normalized difference vegetation indices and partial least squares regression. Remote Sens. Environ. 86, 542–553.

Huete, A., Didan, K., Miura, T., Rodriguez, E.P., Gao, X., Ferreira, L.G., 2002. Overview of the radiometric and biophysical performance of the MODIS vegetation indices. Remote Sens. Environ. 83, 195–213.

Kenny, J.F., Barber, N.L., Hutson, S.S., Linsey, K.S., Lovelace, J.K., Maupin, M.A., 2009. Estimated Use of Water in the United States in 2005 (No. Circular 1344). United State Geological Survey, Reston, VA, p. 52.

Jacquemoud, S., Baret, F., Andrieu, B., Danson, F.M., Jaggard, K., 1995. Extraction of vegetation biophysical parameters by inversion of the PROSPECT+SAIL models on sugar beet canopy reflectance data. Application to TM and AVIRIS sensors. Remote Sens. Environ. 52, 163–172.

Jacquemoud, S., Verhoef, W., Baret, F., Bacour, C., Zarco-Tejada, P.J., Asner, G.P., Francois, C., Ustin, S.L., 2009. PROSPECT + SAIL models: a review of use for vegetation characterization. Remote Sens. Environ. 113 (Supplement 1), S56–S66.

Lu, D., 2006. The potential and challenge of remote sensing-based biomass estimation. Int. J. Remote Sens. 27, 1297–1328.

Mariotto, I., Thenkabail, P.S., Huete, A., Slonecker, E.T., Platonov, A., 2013. Hyperspectral versus multispectral crop-productivity modeling and type discrimination for the HyspIRI mission. Remote Sens. Environ. 139, 291–305.

Marshall, M., Thenkabail, P.S., 2015. Developing in situ non-destructive estimates of crop biomass to address issues of scale in remote sensing. Remote Sens. 7, 808–835.

Marshall, M., Thenkabail, P., 2014. Biomass modeling of four leading world crops using hyperspectral narrowbands in support of HyspIRI Mission. Photogrammetric Eng. Remote Sens. 80, 757–772.

Merton, R., Huntington, J., 1999. Early Simulation Results of the ARIES-1 Satellite Sensor for Multi-Temporal Vegetation Research Derived from AVIRIS. NASA Jet Propulsion Laboratory, Pasadena, CA.

Michaelsen, J., 1987. Cross-validation in statistical climate forecast models. J. Climate Appl. Meteorol. 26, 1589–1600.

Ollinger, S.V., 2011. Sources of variability in canopy reflectance and the convergent properties of plants. New Phytol. 189, 375–394.

Perry, E.M., Roberts, D.A., 2008. Sensitivity of narrow-band and broad-band indices for assessing nitrogen availability and water stress in an annual crop. Agronomy J. 100, 1211–1219.

Richards, J.A., 2013. Correcting and registering images. In: Remote Sensing Digital Image Analysis. Springer, Berlin, New York, NY, pp. 27–77.

Serele, C.Z., Gwyn, Q.H.J., Boisvert, J.B., Pattey, E., McLaughlin, N., Daoust, G., 2000. Corn yield prediction with artificial neural network trained using airborne remote sensing and topographic data. In: Geoscience and Remote Sensing Symposium, vol. 1, pp. 384–386.

Simon, K., 2006. Hyperion Level 1GST (L1GST) Product Output Files Data Format Control Book (DFCB): Earth Observing-1 (EO-1) (No. Version 1.0). United States Geological Survey, Sioux Falls, SD.

Sonnentag, O., Hufkens, K., Teshera-Sterne, C., Young, A.M., Friedl, M., Braswell, B.H., Milliman, T., O'Keefe, J., Richardson, A.D., 2012. Digital repeat photography for phenological research in forest ecosystems. Agric. For. Meteorol. 152, 159–177.

Soulard, C.E., Wilson, T.S., 2013. Recent land-use/land-cover change in the Central California Valley. J. Land Use Sci. http://dx.doi.org/10.1080/1747423X.2013.841297.

Spencer, T., Altman, P., 2010. Climate Change, Water, and Risk: Current Water Demands are not Sustainable. Natural Resources Defense, New York, NY, p. 4.

Stocker, T.F., Qin, D., Plattner, G.-K., Tignor, M., Allen, S.K., Boschung, J., Nauels, A., Xia, Y., Bex, V., Midgley, P.M. (Eds.), 2013. Climate change 2013: the physical science basis. Intergovernmental Panel on Climate Change, Working Group I Contribution to the IPCC Fifth Assessment Report (AR5). Cambridge Univ Press, New York.

Thenkabail, P.S., 2004. Inter-sensor relationships between IKONOS and Landsat-7 ETM+ NDVI data in three ecoregions of Africa. Int. J. Remote Sens. 25, 389–408.

Thenkabail, P.S., Enclona, E.A., Ashton, M.S., Van Der Meer, B., 2004. Accuracy assessments of hyperspectral waveband performance for vegetation analysis applications. Remote Sens. Environ. 91, 354–376.

Thenkabail, P.S., Mariotto, I., Gumma, M.K., Middleton, E.M., Landis, D.R., Huemmrich, K.F., 2013. Selection of Hyperspectral Narrowbands (HNBs) and Composition of hyperspectral twoband vegetation indices (HVIs) for biophysical characterization and discrimination of crop types using field reflectance and hyperion/EO-1 data. IEEE J. Selected Topics Appl. Earth Observations Remote Sens. 6, 427–439.

Thenkabail, P.S., Smith, R.B., De Pauw, E., 2000. Hyperspectral vegetation indices and their relationships with agricultural crop characteristics. Remote Sens. Environ. 71, 158–182.

Thenkabail, P.S., Ward, A.D., Lyon, J.G., Merry, C.J., 1994. Thematic mapper vegetation indices for determining soybean and corn growth parameters. Photogrammetric Eng. Remote Sens. 60, 437–442.

Thorp, K.R., Tian, L., Yao, H., Tang, L., 2004. Narrow-band and derivative-based vegetation indices for hyperspectral data. Trans. ASAE 47, 291–299.

Tu, K.P., 2000. Modeling plant-soil-atmosphere carbon dioxide exchange using optimality principles, PhD. Dissertation. University of New Hampshire, Durham, NH.

Tucker, C.J., 1979. Red and photographic infrared linear combinations for monitoring vegetation. Remote Sens. Environ. 8, 127–150.

Umbach, K.W., 1997. A Statistical Tour of California's Great Central Valley. California Research Bureau, California State Library, Sacramento, CA. Retrieved from: <http://www.library.ca.gov/>.

Ustin, S.L., Roberts, D.A., Gamon, J.A., Asner, G.P., Green, R.O., 2004. Using imaging spectroscopy to study ecosystem processes and properties. Bioscience 54, 523–533.

Vermeulen, S.J., Challinor, A.J., Thornton, P.K., Campbell, B.M., Eriyagama, N., Vervoort, J.M., Smith, D.R., 2013. Addressing uncertainty in adaptation planning for agriculture. Proc. Natl. Acad. Sci. 110, 8357–8362.